Plasmonics
DOI 10.1007/s11468-012-9463-0

The Focusing and Talbot Effect of Periodic Arrays of Metallic Nanoapertures in High-Index Medium

Yiting Yu · Delphine Chassaing · Torsten Scherer · Benjamin Landenberger · Hans Zappe

Received: 18 June 2012 / Accepted: 19 November 2012

Abstract Three finite-sized two-dimensional (2D) periodic arrays of metallic nanoapertures with the shape of nanowave, nanohole, and nanodot have been developed. Using water as an output medium, although the operating wavelengths are larger than the array period, both the focusing and far-field plasmon Talbot effect are experimentally observed, showing a good agreement with the 2D finite-difference time-domain (FDTD) simulation results. The focusing performance in both cases, with the output medium of air and of water, is compared. A detailed investigation of the plasmon Talbot *revivals* reveals that they are composed of subwavelength hotspots with the size of ~0.5λ distributed in the same array period as the original device. Three-dimensional FDTD simulations prove that the existence of surface plasmons (SPs) exhibits an enhanced optical transmission at some SP resonant wavelengths dependent on the output medium. Additionally, it is demonstrated that the Talbot revivals provide a high-resolution mean to distinguish the slight geometric nonuniformity in periodic nanostructures.

Y. Yu (✉)
Key Laboratory of Micro/Nano Systems for Aerospace (Ministry of Education), Northwestern Polytechnical University, Xi'an 710072, People's Republic of China
e-mail: yyt@mail.nwpu.edu.cn

D. Chassaing · T. Scherer
Institute of Nanotechnology (INT), Karlsruhe Nano Micro Facility (KNMF), Karlsruhe Institute of Technology (KIT), Eggenstein-Leopoldshafen 76344, Germany

B. Landenberger
Laboratory for Bio- and Nano-Photonics, Department of Microsystems Engineering–IMTEK, University of Freiburg, Freiburg 79110, Germany

H. Zappe
Laboratory for Micro-optics, Department of Microsystems Engineering–IMTEK, University of Freiburg, Freiburg 79110, Germany

Keywords Surface plasmons · Metallic nanoapertures · Focusing · Talbot effect

Introduction

Since the first discovery of extraordinary optical transmission (EOT) through metallic nanohole arrays [1], surface plasmons (SPs), which exploit the unique optical properties of metallic nanostructures to route and manipulate light at the nanoscale, have attracted tremendous interests in the scientific community [2, 3]. Various plasmonic devices composed of nanoholes [1, 4, 5], nanoparticles [6, 7], nanowires [8, 9], etc. have been developed, and they allow to reduce the size of optical elements for applications such as focusing, waveguiding, sensing, and light trapping [10–12].

Arrays of metallic nanoapertures have been extensively investigated and have become a fundamental plasmonic material showing potentials for sensing [13–15], lensing [16, 17], color filtering [5], etc. Different from the conventional surface plasmon resonance (SPR) devices based on a continuous metal film allowing only surface plasmon polaritons (SPPs) [18], due to the periodic nature of these metallic nanoapertures, a complicated coupling behavior exhibits between the localized surface plasmon resonance (LSPR) in the apertures, the Bloch wave surface plasmon polaritons (BW-SPPs), and Wood's anomalies. This coupling behavior results in the EOT feature at some resonant wavelengths and makes it a difficult task to precisely predict the transmission properties of periodic SP devices in theory if considering various parameters that may affect the ultimate results, including the film thickness [19], geometric shape and size [20, 21], periodicity and lattice type [22] of nanoapertures, polarizations of illumination [5], characteristics of metal/dielectric interfaces [13], and so on.

In this paper, we firstly investigate the lensing effect of finite-sized two-dimensional (2D) periodic arrays of

Published online: 30 November 2012

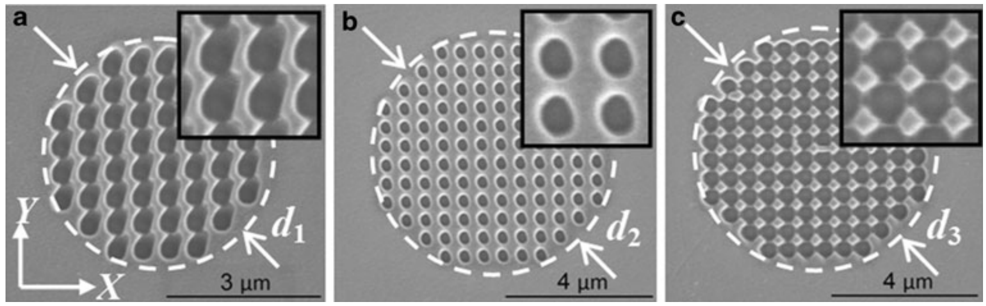

Fig. 1 Scanning electron microscopy (SEM) images of the fabricated finite-sized 2D periodic arrays of metallic nanoapertures: **a** nanowaves (#1); **b** nanoholes (#2); and **c** nanodots (#3). The insets give the details of nanoapertures

metallic nanoapertures having the same dimensions, which are similar to the patches of nanoholes suggested by Gao et al [17]. Three distinct shapes of nanoapertures named nanowave, nanohole, and nanodot, respectively, are analyzed. In addition to observing the focusing property in the air, as reported in most literature [16, 17, 23–25], we also perform an investigation using an output medium with a higher refractive index, which is rarely discussed in publications. The focusing capability of the periodic arrays of metallic nanoapertures in a high-index medium shows potentials for immersion lithography [26] and some optofluidic applications [27, 28]. From our experimental results, not only the excellent focusing behavior is realized, but also the far-field Talbot effect, a famous self-imaging phenomenon from the classical optics, is clearly seen, even when the operating wavelengths are larger than the array period, in which case the Talbot effect should not occur according to Gao et al [17].

The conventional Talbot effect of a diffraction grating illuminated by a monochromatic plane wave was discovered by Talbot in 1836 [29] and first explained analytically by Rayleigh in 1881 [30], attributing its origin to the interference of diffracted beams. Accordingly, the repeated self-images (*revivals*) to the initial grating configuration at multiples of a characteristic distance (the Talbot distance τ, given by $\tau=2a^2/\lambda$ in the paraxial approximation, where a is the grating period and λ the wavelength) from the grating surface can be obtained. The Talbot effect promises applications ranging from optical computing [31], phase locking of laser arrays [32], atomic waves [33], optical fiber systems [34], to waveguide arrays [35].

In recent years, the analogue of the Talbot effect has been studied theoretically [36–39] and experimentally [40–42] for SPPs. Plasmon Talbot carpets containing rich subwavelength hotspots are shown. However, most research focuses on one-dimensional arrays of nanostructures, e.g., nanoholes [36, 42], nanoslits [38, 40], and nanoparticles [37, 41], so only the 2D plasmon Talbot revivals can be achieved. Meanwhile, the Talbot effect in the above research appears in the near-field zone of the metal/dielectric

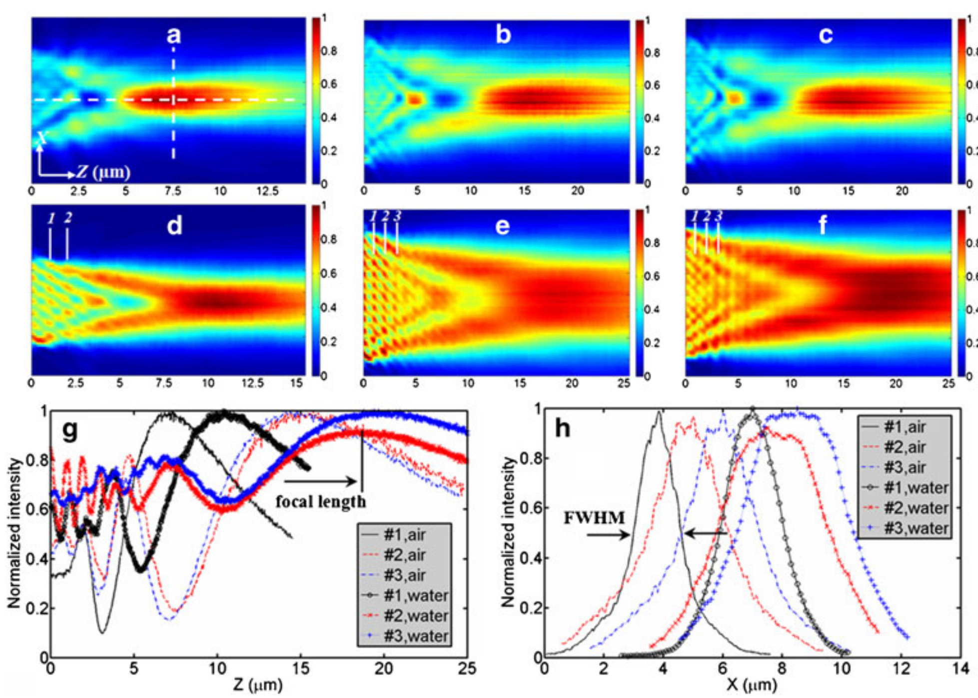

Fig. 2 Experimental results of the output optical field in *X*–*Z* plane when the devices were illuminated by an incident light of 623 nm in wavelength. The output medium is **a**–**c** air and **d**–**f** water. **a** and **d**, **b** and **e**, and **c** and **f** are for the nanowave-, nanohole-, and nanodot-arrayed devices, respectively. **g**, **h** The derived intensity profiles for all the cases along the *white dashed lines* passing through the focal points in the two directions, as shown in **a**. The intensity is normalized for the output of each device. For clarity, the intensity profiles for the cases **b**–**f** in **h** are shifted by 1 to 5 μm in *x*-axis, respectively

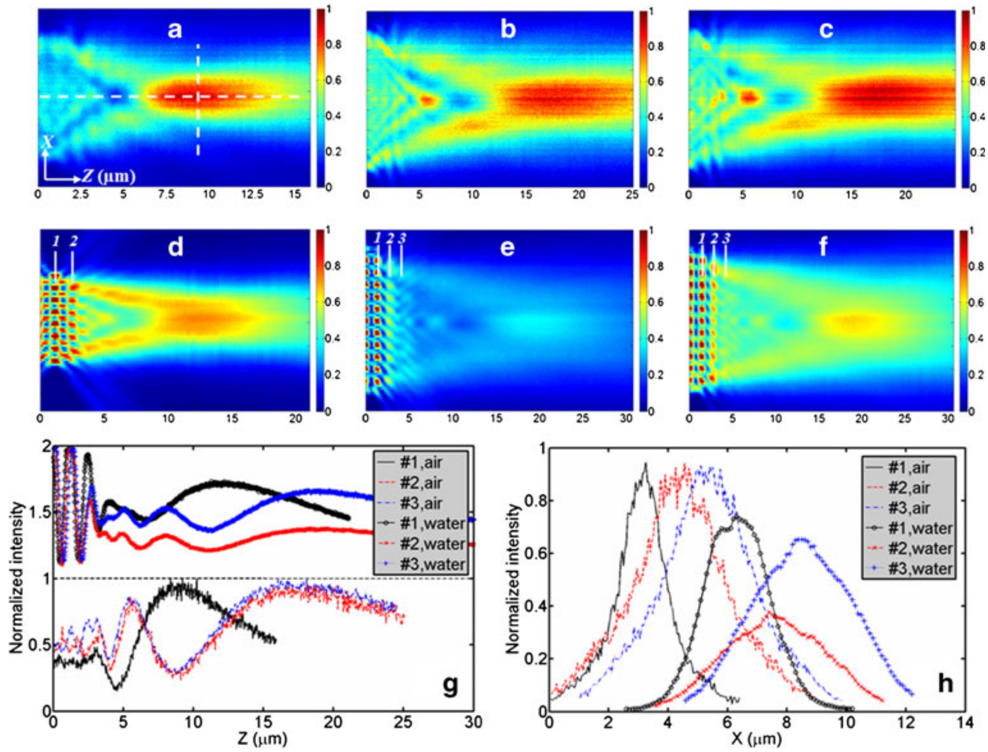

Fig. 3 Experimental results of the output optical field in *X–Z* plane when the devices were illuminated by an incident light of 525 nm in wavelength. The output medium is **a**–**c** air and **d**–**f** water. **a** and **d**, **b** and **e**, and **c** and **f** are for the nanowave-, nanohole-, and nanodot-arrayed devices, respectively. **g**, **h** The derived intensity profiles for all the cases along the *white dashed lines* passing through the focal points in the two directions, as shown in **a**. The intensity is normalized for the output of each device. For clarity, the intensity profiles for the cases **d**–**f** in **g** are shifted by 1 in *y*-axis, and those for cases **b**–**f** in **h** are shifted by 1 to 5 μm in *x*-axis, respectively

interface, and the resulting plasmon Talbot revivals are distributed along the interface. Li et al [39] theoretically studied the three-dimensional (3D) plasmon Talbot effect of a nanolens composed of nanorings, and the surveyed plasmon Talbot effect spans from the near field to the far field. To the best of our knowledge, experimental investigation on 3D far-field plasmon Talbot effect has not yet been reported.

Experimental Results

The scanning electron microscopy images of the three finite-sized 2D periodic arrays of metallic nanoapertures with the shape of nanowave, nanohole, and nanodot, respectively, are shown in Fig. 1. All the devices were fabricated by focused ion beam milling in a 200-nm gold film on a Pyrex wafer and with the same array period of 500 nm in both *X* and *Y* directions. The nanoholes are ~250 nm in diameter. The nanoapertures are in square lattice to form an approximate circular pattern, with the diameter d_1−d_3 of 4.5, 6.2, and 6.2 μm, respectively. For simplicity in the following discussion, the nanowave-, nanohole-, and nanodot-arrayed devices are denoted as #1, #2, and #3, respectively.

Focusing

The experimental results of the output optical field in *X–Z* plane for all the three devices in both air and water (refractive index n=1.33) are shown in Figs. 2 and 3, for the operating wavelength of 623 and 525 nm, respectively. In the following context, we will use λ_623 and λ_525 for these two wavelengths.

From Figs. 2 and 3, obvious focusing behavior can be observed for all the three devices under different conditions. Therefore, not only the arrays of metallic nanoholes as suggested by Gao et al [17], but also the arrays composed of arbitrary metallic nanoapertures in a subwavelength periodicity can focus the incident light. The resulted focal lengths for all cases, derived from the intensity profiles

Table 1 Comparison of the measurement and calculation results of focal lengths for the nanowave-, nanohole-, and nanodot-arrayed devices under different working conditions (unit in micrometer)

Device	Air, λ_623		Air, λ_525		Water, λ_623		Water, λ_525	
	Exp.	Cal.	Exp.	Cal.	Exp.	Cal.	Exp.	Cal.
#1	7.48	8.13	9.18	9.64	10.38	10.81	12.15	12.83
#2	15.25	15.43	17.96	18.30	18.65	20.52	19.54	24.35
#3	14.72	15.43	17.58	18.30	19.18	20.52	19.25	24.35

shown in Figs. 2g and 3g, are listed in Table 1. In our experiments, the output optical intensity for λ_525 is greatly smaller than that for λ_623.

Using the Rayleigh–Sommerfeld integral, the theoretical focal length when a plane wave of wavelength λ incidents on a circular aperture of radius ρ can be calculated by [43]

$$I(Z) = 4I_0 \sin\left(\frac{\pi\rho^2}{2\lambda Z}\right)^2 \tag{1}$$

where I_0 is the initial intensity of the wave, and $I(Z)$ is the output intensity along the optical axis at a distance Z away from the aperture. Thus, the focal point, defined as the point of maximal output intensity, can be written as Z_m, which equals to ρ^2/λ. The calculated focal lengths are also listed in Table 1. The effective wavelength (λ/n; n, refractive index) in the case of water as an output medium are 468 and 395 nm for λ_623 and λ_525, respectively.

From Table 1, the measurement results are in good accordance with the theoretical predictions, though the former is always smaller than the latter. The main reason is that the geometry of all the devices is in fact octagonal, slightly smaller than the circle used for the calculations.

Besides the focal length, the full width at half maximum (FWHM) of the focal point can also be derived from the intensity profiles as shown in Figs. 2h and 3h. For λ_623, the FWHMs of the three devices are 1.61, 2.87, and 2.64 µm in air, and 2.19, 4.08, and 3.92 µm in water. While for λ_525, the FWHMs are 1.62, 3.21, and 3.29 µm in air, and 2.57, 4.09, and 4.28 µm in water. As a result, when a finite-sized 2D periodic array of metallic nanoapertures works in a high-index medium, both the focal length and FWHM of the focus will be enlarged.

Far-Field Plasmon Talbot Effect

From the output optical fields as shown in Figs. 2d–f and 3d–f, the far-field plasmon Talbot effect is also clearly observed. From Figs. 2a–c and 3a–c, as the operating wavelengths (623 and 525 nm) are slightly larger than the array period (500 nm) in the air, all the high-order diffractions are suppressed when the devices are illuminated, so that the interference of diffracted beams, further resulting in the

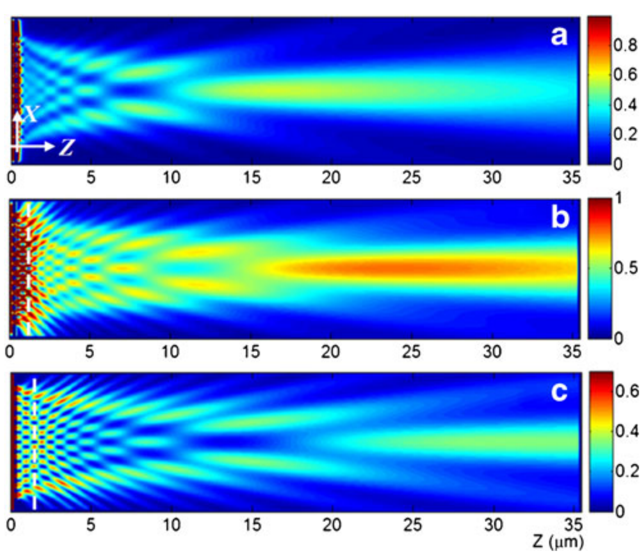

Fig. 4 2D FDTD simulation results of a subwavelength grating in a 200-nm gold film. The period and slit width are 500 and 250 nm, respectively. A TM-polarized plane wave propagates from the left. The settings in the simulation are: **a** air, λ_623; **b** water, λ_623; and **c** water, λ_525. To show the output optical field clearly, the electric-field intensity inside the nanoslits is saturated. The light intensity for **c** is magnified by 10

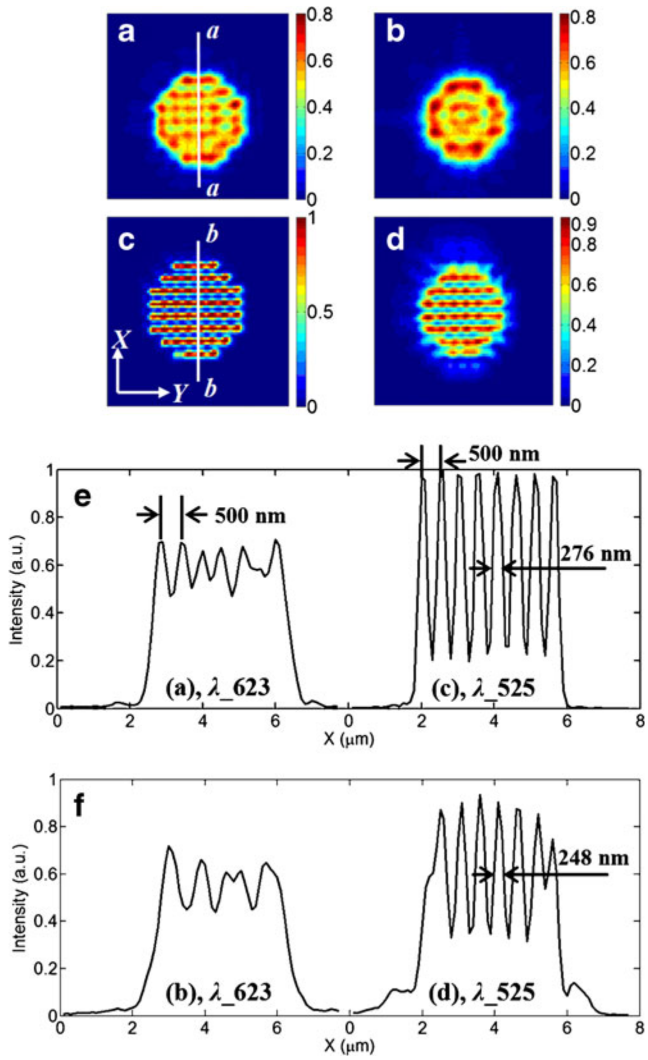

Fig. 5 **a**–**d** The optical fields parallel to X–Y plane at two different distances (τ and 2τ) from the output surface of the nanowave-arrayed device, denoted as cross sections 1 and 2 in Figs. 2d and 3d: **a** cross section 1, λ_623; **b** cross section 2, λ_623; **c** cross section 1, λ_525; **d** cross section 2, λ_525. The derived intensity profiles along the *white solid lines*, *a*–*a* of **a** and **b**, and *b*–*b* of **c** and **d**, are shown in **e** and **f**, corresponding to the cross sections 1 and 2, respectively

self-imaging Talbot effect, will not occur, as demonstrated by Gao et al [17]. However, using water as an output medium, the resulted effective wavelengths (468 and 395 nm) become smaller than the array period, making the high-order diffractions present and ultimately the Talbot effect. As a consequence, by utilizing a high-index medium of refractive index n, the operating wavelength for achieving the Talbot effect will be broadened, increased by a factor of n–1 theoretically.

From the experimental measurements (Figs. 2 and 3), we found that the Talbot distance largely depends on the wavelength for a specific array period. The measured Talbot distances are 0.95 and 1.18 μm for λ_623 and λ_525, respectively. In the quasi-near-field zone of the devices, the propagating plasmons revive the device patterns quite well. As the distance from the device surface increases, the Talbot revivals get worse, and the intensity decreases due to the propagation loss. For a larger array (with more nanoapertures), the Talbot revivals are more pronounced and the intensity decays more slowly. A shorter operating wavelength will also make the Talbot effect more obvious. However, as the Talbot effect becomes more pronounced, the relative light intensity of the focusing part (divided by the total output) gets weaker.

To verify the experimental results, 2D finite-difference time-domain (FDTD) simulations were performed, giving the output optical fields for different working conditions. A subwavelength grating composed of nanoslits having the same geometric sizes as the nanohole-arrayed device (#2) was analyzed under illumination of a TM-polarized plane wave. Figure 4 shows the simulation results, from which we can see that for λ_623, no obvious Talbot effect can be observed in the air (Fig. 4a). However, using water as the output medium, the Talbot revivals for the same wavelength are achieved with the Talbot distance of 0.75 μm (from the dashed line to the device surface as shown in Fig. 4b). Further reducing the wavelength to 525 nm, the more pronounced Talbot revivals are realized (Fig. 4c), with the Talbot distance of 1.0 μm. Nonetheless, the output light intensity is greatly weakened. The simulation results agree well with the experiments, though the simulated Talbot distances are slightly smaller than the measurements.

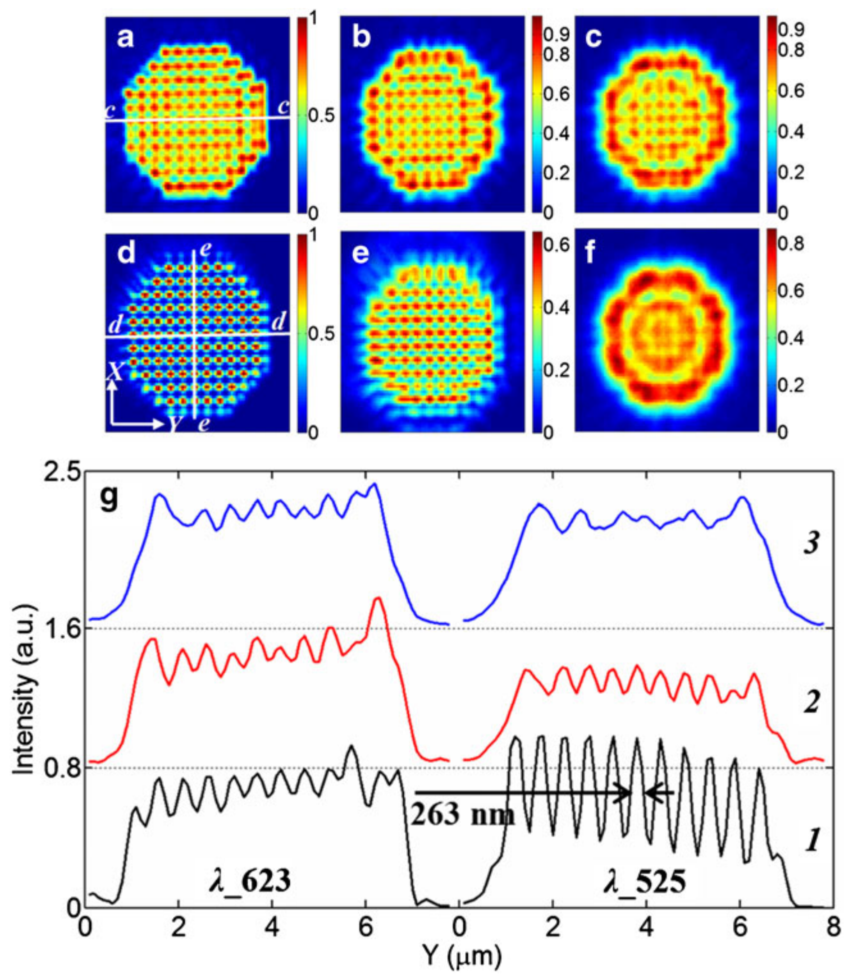

Fig. 6 **a**–**f** The optical fields parallel to X–Y plane at three different Talbot distances (τ, 2τ, and 3τ) from the output surface of the nanohole-arrayed device, denoted as cross sections 1–3 in Figs. 2e and 3e: **a**–**c** for λ_623, cross section 1 to 3, respectively; **d**–**f** for λ_525, cross section 1 to 3, respectively. The derived intensity profiles along the *white solid lines*, *c*–*c* of **a**–**c** and *d*–*d* of **d**–**f**, are shown in **g**. The intensity at the cross sections *2* and *3* is shifted by 0.8 and 1.6, respectively

According to the definition of the Talbot distance ($\tau=2a^2/\lambda$), the calculated Talbot distances in the water are 1.067 and 1.267 μm for λ_623 and λ_525, respectively. Obviously, the calculated values are larger than both the simulations and measurements, which agrees with the previous research [40–42], mentioning that when the operating wavelength is comparable to the array period, the practical Talbot distance will be slightly smaller than the value achieved in the paraxial approximation. Oosten et al [42] suggested a modified formula to estimate the Talbot distance when the array period is less than 2λ,

$$\tau = \frac{\lambda}{1-\sqrt{1-(\lambda/a)^2}} \tag{2}$$

which in the limit of a approaching infinity, τ equals to $2a^2/\lambda$. Therefore, the calculated Talbot distances in the water for Fig. 4b, c are 0.72 and 1.02 μm, respectively. These results coincide well with the simulations. As for the slightly larger measured values, we suppose the 2D periodic array to be responsible. For the fabricated devices, in addition to the periodicities in X and Y directions, periodicities in ±45° directions are also present, where the array period is ~707 nm. Thus, the ultimate optical field is actually a combination of these two arrays.

Figure 5a–d shows the derived optical fields parallel to X–Y plane at two different distances from the output surface of the nanowave-arrayed device, denoted as cross sections 1 and 2 in Figs. 2d and 3d. Figure 5a, b is for λ_623, and Fig. 5c, d is for λ_525. Cross sections 1 and 2 are located at the first two Talbot distances (τ and 2τ). Obviously, the Talbot revivals, imitating the device pattern, are observed. The shorter the wavelength is, the more pronounced the Talbot revivals are. Along the white solid lines, a–a and b–b, intensity profiles are extracted and shown in Fig. 5e, f. We can see that the Talbot revivals have exactly the same array period as the device. The more pronounced Talbot revivals imply a higher contrast in the intensity. The FWHM of the obtained Talbot nanowaves in Fig. 5c is ~276 nm (0.526λ). Interestingly, at the second Talbot distance (Fig. 5d), the FWHM becomes even smaller, decreasing to ~248 nm (0.472λ). Therefore, the hotspots in the plasmon Talbot revivals possess a far better resolution than the focusing discussed in the previous section.

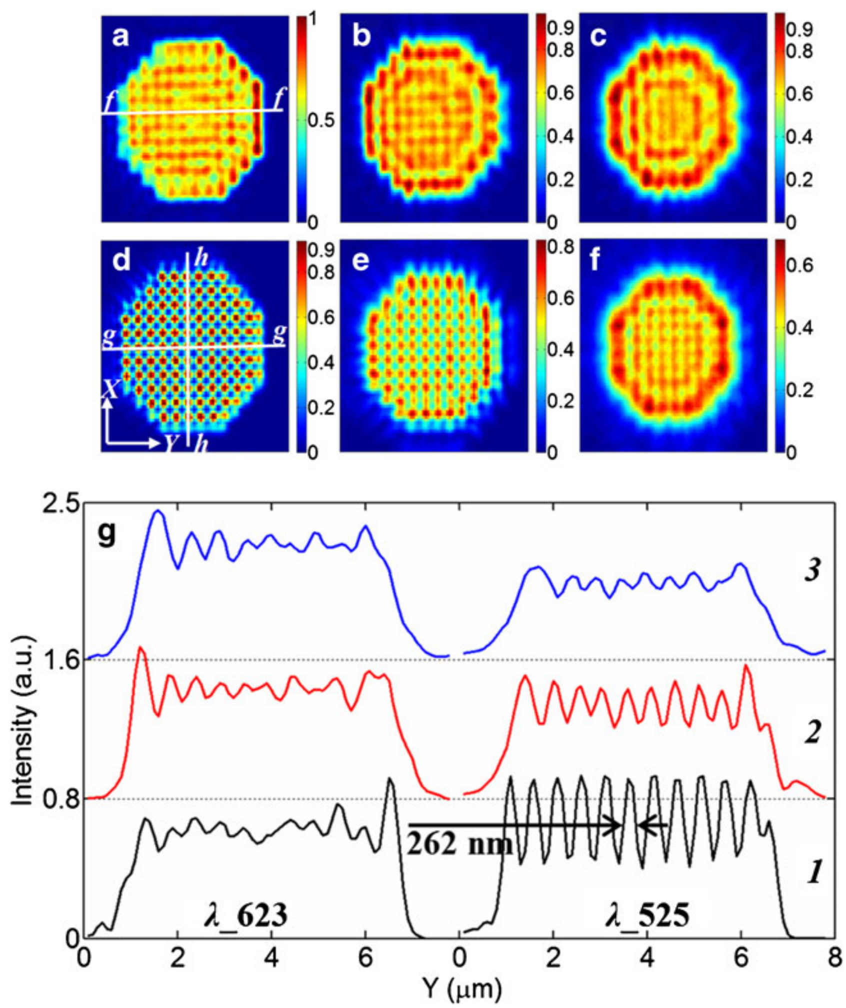

Fig. 7 **a**–**f** The optical fields parallel to X–Y plane at three different Talbot distances (τ, 2τ, and 3τ) from the output surface of the nanodot-arrayed device, denoted as cross sections 1–3 in Figs. 2f and 3f: **a**–**c** for λ_623, cross section 1 to 3, respectively; **d**–**f** for λ_525, cross section 1 to 3, respectively. The derived intensity profiles along the *white solid lines*, *f*–*f* of **a**–**c** and *g*–*g* of **d**–**f**, are shown in **g**. The intensity at the cross sections *2* and *3* is shifted by 0.8 and 1.6, respectively

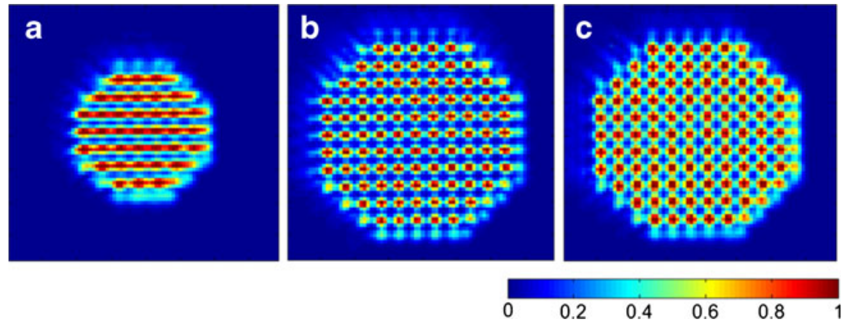

Fig. 8 Plasmon Talbot *fractional revivals* derived at a position 1.5τ for the three devices for λ_525: **a** nanowave-arrayed; **b** nanohole-arrayed; **c** nanodot-arrayed. Compared to Figs. 5c, 6d, and 7d, almost the same Talbot *revivals* are achieved but displaced by half the array period (250 nm) in the *X–Y* plane

Figures 6 and 7 show similar results for the nanohole- and nanodot-arrayed devices, in which the cross section 3 is located at the third Talbot distance (3τ). The plasmon Talbot revivals with both transversal and longitudinal periodic distributions of hotspots are achieved. FWHMs of the hotspots in these two cases are ~263 and ~262 nm (~0.5λ), respectively.

As reported previously [36, 37, 40–42], in addition to the Talbot revivals at integral Talbot distances, *fractional revivals* at *fractional* Talbot distances (1/2τ, 3/2τ…) also exist. Figure 8 presents the plasmon Talbot fractional revivals achieved at a position 1.5τ for the three devices for λ_525. These fractional revivals reveal almost the same patterns as their first integral Talbot revivals, but with a lateral shift of half the array period (250 nm) in the *X–Y* plane.

Discussions

As demonstrated in previous research, finite-sized 2D periodic arrays of metallic nanoholes [17] or nanocrosses [16] show an excellent focusing capability. However, the significant influence of diffraction existing in the micrometer-scale devices makes the focal point subject to the classical diffraction limit because the far-field focusing does not originate from the evanescent field recovery [44] nor super-oscillations [24]. This is proved by our measurements, and the sizes (FWHMs) of focal points derived are similar to the existing reports [16, 17, 23].

On the other hand, when all the nanoapertures have the same dimensions, the design and fabrication of the devices will become easier, as the focusing effect in this case is not a consequence of curved wavefront [16, 23] but comes from the interference of in-phase electromagnetic waves, which is a direct result of the excitation of SPs in the nanoapertures [17]. Therefore, the final focal length is mainly determined by the overall diameter of the device, while the optical throughput and the intensity of the focal point depend sensitively on the SPR wavelengths (showing an EOT phenomenon) determined by the substructures.

As described, due to the complicated coupling behavior between LSPR, BW-SPPs, and Wood's anomalies, an accurate theoretical model to predict the transmissivity at different wavelengths is still not available. Therefore, we utilized the 3D FDTD method to perform a full-field electromagnetic simulation to get the transmission property for the nanohole-arrayed device. The simulation results are given in Fig. 9. The simulated structure, as the inset shows, has the same geometric dimensions and lattice type as the device #2. The output medium was taken to be water at first. The achieved broadband spectrum (solid line) indicates two SPR wavelengths, 612 and 869 nm, over the wavelength range from 500 nm to 1 μm. The highly SP-enhanced optical transmission (EOT) appears at the second SPR wavelength, with the transmissivity of 28.3 %, while the fraction of surface area occupied by the nanoholes is ~19.6 %. The operating wavelength of 623 nm is closer to the shorter SPR wavelength, correspondingly showing a higher optical transmission than λ_525, which explains our experimental results in Figs. 2 and 3. Then, changing the output medium to glycerin (refractive index of 1.47, dashed line), the two

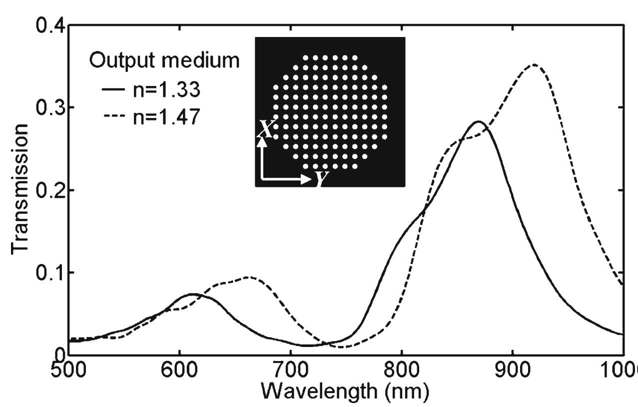

Fig. 9 3D FDTD simulation results of the transmission property for the nanohole-arrayed device. The output medium is water with a refractive index of 1.33 (*solid line*), and glycerin with a refractive index of 1.47 (*dashed line*) to match the refractive index of Pyrex wafer. The *inset* is a plot of the permittivity of the simulated device in the *X–Y* plane, with the array period of 500 nm and nanohole diameter of 250 nm

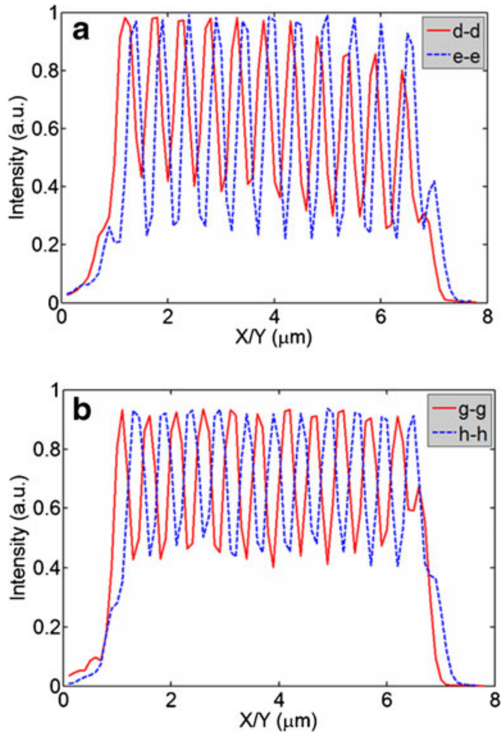

Fig. 10 Comparison of intensity profiles in both X and Y directions to distinguish the slight geometric nonuniformity existing in original devices, for the plasmon Talbot *revivals* of **a** (Fig. 6d) and **b** (Fig. 7d)

SPR wavelengths are both red-shifted to 663 and 919 nm, and the transmissivity at the second SPR wavelength increases to 35.2 %. This result is well consistent with previous research [13, 45], revealing an index-matching effect of plasmonic devices, as the refractive index of the Pyrex substrate is also 1.47.

Gao et al [17] did not observe the Talbot effect of their plasmonic patches, and they attributed it to the finite size of nanohole arrays. From our research, the reason is that working in the air, the operating wavelengths they used are larger than the array periods of their devices. With a high-index output medium, though in a similar situation, we observed the far-field plasmon Talbot effect, revealing Talbot revivals and fractional revivals with subwavelength hotspots. However, the Talbot effect is a diffraction-related phenomenon, and the far-field Talbot revivals do not take advantage of the near-field evanescent wave, making the hotspots still diffraction-limited, as demonstrated in this research. In spite of this, the FWHMs of hotspots are close to 0.5λ, largely smaller than the size of focal points. Accompanied by the periodic property, the plasmon Talbot effect can be exploited for the 2D and 3D low-cost nanolithography.

To overcome the diffraction limit, an optimized design of the periodic arrays of metallic nanoapertures is needed. One way is to make the focal point or the first Talbot revival as close as possible to the device surface to enter the near-field zone because the SPs propagating distance (when the amplitude decreases to $1/e$) in the dielectric is also in the same order. For instance, at a wavelength of 600 nm, the calculated SPs propagating distance in the air is 390 nm for silver and 280 nm for gold [46]. By this method, Shi et al [47] designed a silver plasmonic lens of the focal length 0.6 μm, and at the 650 nm wavelength, the FWHM of the realized focal point was 270 nm (~0.415λ). Li et al [39] investigated the Talbot effect of a silver plasmonic nanolens, and for the operating wavelength of 248 nm, the size of the first Talbot hotspots was 100 nm (~0.403λ) at a propagating distance of 396 nm.

From Figs. 5, 6, and 7, we can see that the plasmon Talbot revivals revive the device pattern extremely well, especially for λ_525 at the first Talbot distance. More surprisingly, even a slight geometric nonuniformity in periodic arrays of nanostructures can be distinguished by analyzing the intensity profiles along different directions. Figure 10 compares the intensity profiles in both X and Y directions of the achieved Talbot revivals as shown in Figs. 6d and 7d. In Fig. 10a, due to the slightly elliptical shape (long axis in Y direction) of the nanoholes, as the inset in Fig. 1b shows, the intensity profile in X direction (e–e) shows a better contrast than that in Y direction (d–d). As the nanodot-arrayed device has a better uniformity in both directions, a similar contrast in the intensity profiles along g–g and h–h directions is achieved (see Fig. 10b). The sensitivity of intensity profile

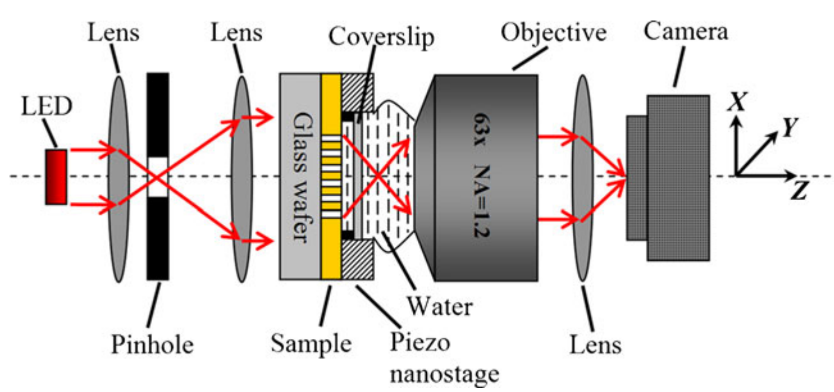

Fig. 11 Experimental setup to record the output optical fields of the samples illuminated by an unpolarized monochromatic light. The piezo nanostage is moved automatically at a 25-nm step in Z direction. For every movement of nanostage, the 2D optical field parallel to X–Y plane is imaged by a CCD camera

to the geometric nonuniformity indicates a possibility of controlling the contrast of the plasmon Talbot revivals via the fill factor, defined as the ratio between the size of nanoapertures and the array period.

Experimental Methods

Optical Characterizations

The output optical fields of the samples in our research were measured using the experimental setup as illustrated schematically in Fig. 11. An inverted microscope (Axiovert 200M, *Zeiss*) was used as a main platform to record the transmitted lights through the samples, which were illuminated from the substrate side with two unpolarized monochromatic light sources. The standard LED modules (Edixeon, 1W, *Edison Opto*) of wavelengths 623 nm (red) and 525 nm (green) were adopted for illumination. The samples were mounted on a *XYZ* piezo nanostage (MCL, *Nano-LP*) with the optical axis oriented along the *Z* direction. The nanostage was controlled by a self-designed software based on the Python programming language, and the pre-set step size for scanning in *Z* direction was 25 nm. The transmitted light in the air was collected by a ×100 objective (NA=0.9, Zeiss) and that in the water by a ×63 objective (NA=1.2, Zeiss), and later imaged on a CCD camera.

Simulations

The 2D and 3D electromagnetic simulations for the output optical fields of a subwavelength grating (Fig. 4) and the transmission property of the nanohole-arrayed device (Fig. 9) were performed using MEEP [48], a freely available software package based on the FDTD method. The boundary condition of the simulated area or volume was set to perfect matched layer to adsorb the scattering light. All the computations were done on a personal computer (CPU: Dual-Core, 2.7 GHz; RAM 4 GB), and a maximum number of elements was limited to about ten millions. The permittivity of gold was modeled by the Drude–Lorentz method, and the related parameters were referred to ref. [49] but modified according to a setting unit length of 200 nm. The plane to calculate the transmitted light intensity was positioned 1 μm away from the device surface.

Summary

In summary, three finite-sized 2D periodic arrays of metallic nanoapertures with the shape of nanowave, nanohole, and nanodot were developed. Using water as the output medium, not only the focusing was realized but also the plasmon Talbot effect was clearly observed in case of a larger operating wavelength than the array period. The latter was previously thought to be impossible when considering the air as the output medium. As both the focusing and Talbot revivals were achieved in the far-field zone of the devices, the sizes of the focal points and Talbot hotspots were diffraction-limited. However, the size of Talbot hotspots was close to 0.5λ. With an optimized design of the plasmonic devices to take advantage of the evanescent field, a higher resolution of the optical spots beyond the diffraction limit may be implemented. This is a research topic of ongoing interest. The existence of SPs greatly enhances the optical transmission at some SPR wavelengths. The focusing capability and miniaturization of the planar plasmonic devices allow the integration into many existing systems for a variety of applications such as imaging, light trapping, etc. While the self-imaging Talbot effect may find a promising application for the 2D and 3D low-cost, high-yield nanolithography [50, 51].

Acknowledgments We thank Lars Friedrich for his help in performing the first optical characterization. We acknowledge the financial support by the Postdoctoral Research Fellowship from the Alexander von Humboldt Foundation, Germany. This work was partially carried out with the support of the Karlsruhe Nano Micro Facility (www.knmf.kit.edu), a Helmholtz Research Infrastructure at Karlsruhe Institute of Technology (www.kit.edu).

References

1. Ebbesen TW, Lezec HJ, Ghaemi HF, Thio T, Wolff PA (1998) Extraordinary optical transmission through sub-wavelength hole arrays. Nature 391:667–669
2. Barnes WL, Dereux A, Ebbesen TW (2003) Surface plasmon subwavelength optics. Nature 424:824–830
3. Ozbay E (2006) Plasmonics: merging photonics and electronics at nanoscale dimensions. Science 311:189–193
4. Coe JV, Heer JM, Teeters-Kennedy S, Tian H, Rodriguez KR (2008) Extraordinary transmission of metal films with arrays of subwavelength holes. Annu Rev Phys Chem 59:179–202
5. Lee MH, Gao H, Henzie J, Odom TW (2007) Microscale arrays of nanoscale holes. Small 3(12):2029–2033
6. Tamada K, Nakamura F, Ito M, Li XH, Baba A (2007) SPR-based DNA detection with metal nanoparticles. Plasmonics 2(4):185–191
7. Yong KT, Swihart MT, Ding H, Prasad PN (2009) Preparation of gold nanoparticles and their applications in anisotropic nanoparticle synthesis and bioimaging. Plasmonics 4(2):79–93
8. Staleva H, Skrabalak SE, Carey CR, Kose T, Xia Y, Hartland GV (2009) Coupling to light, and transport and dissipation of energy in silver nanowires. Phys Chem Chem Phys 11:5889–5896
9. Cao L, Nome RA, Montgomery JM, Gray SK, Scherer NF (2010) Controlling plasmonic wave packets in silver nanowires. Nano Lett 10(9):3389–3394
10. Lal S, Link S, Halas NJ (2007) Nano-optics from sensing to waveguiding. Nat Photonics 1:641–648
11. Kawata S, Inouye Y, Verma P (2009) Plasmonics for near-field nano-imaging and superlensing. Nat Photonics 3:388–394

12. Atwater HA, Polman A (2010) Plasmonics for improved photovoltaic devices. Nat Mater 9:205–213
13. McMahon JM, Henzie J, Odom TW, Schatz GC, Gray SK (2007) Tailoring the sensing capabilities of nanohole arrays in gold films with Rayleigh anomaly surface plasmon polaritons. Opt Express 15(26):18119–18129
14. McPhillips J, Murphy A, Jonsson MP, Hendren WR, Atkinson R, Höök F, Zayats AV, Pollard RJ (2010) High-performance biosensing using arrays of plasmonic nanotubes. ACS Nano 4(4):2210–2216
15. Sannomiya T, Scholder O, Jefimovs K, Hafner C, Dahlin AB (2011) Investigation of plasmon resonances in metal films with nanohole arrays for biosensing applications. Small 7(12):1653–1663
16. Lin L, Goh XM, McGuinness LP, Roberts A (2010) Plasmonic lenses formed by two-dimensional nanometric cross-shaped aperture arrays for Fresnel-region focusing. Nano Lett 10(5):1936–1940
17. Gao H, Hyun JK, Lee MH, Yang JC, Lauhon LJ, Odom TW (2010) Broadband plasmonic microlenses based on patches of nanoholes. Nano Lett 10(10):4111–4116
18. Homola J, Yee SS, Gauglitz G (1999) Surface plasmon resonance sensors: review. Sensors Actuators B 54:3–15
19. Degiron A, Lezec HJ, Barnes WL, Ebbesen TW (2002) Effects of hole depth on enhanced light transmission through subwavelength hole arrays. Appl Phys Lett 81(23):4327–4329
20. Kim JH, Moyer PJ (2006) Transmission characteristics of metallic equilateral triangular nanohole arrays. Appl Phys Lett 89:121106
21. Klein Koerkamp KJ, Enoch S, Segerink FB, van Hulst NF, Kuipers L (2004) Strong influence of hole shape on extraordinary transmission through periodic arrays of subwavelength holes. Phys Rev Lett 92(18):183901
22. Thio T, Ghaemi HF, Lezec HJ, Wolff PA, Ebbesen TW (1999) Surface-plasmon-enhanced transmission through hole arrays in Cr films. J Opt Soc Am B 16(10):1743–1748
23. Verslegers L, Catrysse PB, Yu Z, White JS, Barnard ES, Brongersma ML, Fan S (2009) Planar lenses based on nanoscale slit arrays in a metallic film. Nano Lett 9(1):235–238
24. Huang FM, Kao TS, Fedotov VA, Chen Y, Zheludev NI (2008) Nanohole array as a lens. Nano Lett 8(8):2469–2472
25. Wang J, Zhou W (2010) Experimental investigation of focusing of gold planar plasmonic lenses. Plasmonics 5(6):325–329
26. Owa S, Nagasaka H (2004) Advantage and feasibility of immersion lithography. J Microlith Microfab Microsyst 3(1):97–103
27. Psaltis D, Quake SR, Yang C (2006) Developing optofluidic technology through the fusion of microfluidics and optics. Nature 442:381–386
28. Monat C, Domachuk P, Eggleton BJ (2007) Integrated optofluidics: a new river of light. Nat Photonics 1:106–114
29. Talbot HF (1836) Facts relating to optical science, No. IV. Philos Mag 9:401–407
30. Rayleigh L (1881) On copying diffraction-gratings, and on some phenomena connected therewith. Philos Mag 11(67):196–205
31. Patorski K (1989) The self imaging phenomenon and its applications. Prog Opt 27:1–108
32. Liu L (1989) Lau cavity and phase locking of laser arrays. Opt Lett 14(23):1312–1314
33. Chapman MS, Ekstrom CR, Hammond TD, Schmiedmayer J, Tannian BE, Wehinger S, Pritchard DE (1995) Near-field imaging of atom diffraction gratings: the atomic Talbot effect. Phys Rev A 51(1):R14–R17
34. Azaña J (2005) Spectral Talbot phenomena of frequency combs induced by cross-phase modulation in optical fibers. Opt Lett 30 (3):227–229
35. Iwanow R, May-Arrioja DA, Christodoulides DN, Stegeman GI, Min Y, Sohler W (2005) Discrete Talbot effect in waveguide arrays. Phys Rev Lett 95:053902
36. Dennis MR, Zheludev NI, García de Abajo FJ (2007) The plasmon Talbot effect. Opt Express 15(15):9692–9700
37. Maradudin AA, Leskova TA (2009) The Talbot effect for a surface plasmon polariton. New J Phys 11:033004
38. Wang Y, Zhou K, Zhang X, Yang K, Wang Y, Song Y, Liu S (2010) Discrete plasmonic Talbot effect in subwavelength metal waveguide arrays. Opt Lett 35(5):685–687
39. Li L, Fu Y, Wu H, Zheng L, Zhang H, Lu Z, Sun Q, Yu W (2011) The Talbot effect of plasmonic nanolenses. Opt Express 19 (20):19365–19373
40. Zhang W, Zhao C, Wang J, Zhang J (2009) An experimental study of the plasmonic Talbot effect. Opt Express 17(22):19757–19762
41. Cherukulappurath S, Heinis D, Cesario J, van Hulst NF, Enoch S, Quidant R (2009) Local observation of plasmon focusing in Talbot carpets. Opt Express 17(26):23772–23784
42. Oosten D, Spasenović M, Kuipers L (2010) Nanohole chains for directional and localized surface plasmon excitation. Nano Lett 10 (1):286–290
43. Ruffieux P, Scharf T, Herzig HP, Völkel R, Weible KJ (2006) On the chromatic aberration of microlenses. Opt Express 14(11):4687–4694
44. Liu Z, Durant S, Lee H, Pikus Y, Fang N, Xiong Y, Sun C, Zhang X (2007) Far-field optical superlens. Nano Lett 7(2):403–408
45. Lee HS, Yoon YT, Lee SS, Kim SH, Lee KD (2007) Color filter based on a subwavelength patterned metal grating. Opt Express 15 (23):15457–15463
46. Raether H (1988) Surface plasmons. Springer, Berlin, p 6
47. Shi H, Wang C, Du C, Luo X, Dong X, Gao H (2005) Beam manipulating by metallic nano-slits with variant widths. Opt Express 13(18):6815–6820
48. Oskooi AF, Roundy D, Ibanescu M, Bermel P, Joannopoulos JD, Johnson SG (2010) MEEP: a flexible free-software package for electromagnetic simulations by the FDTD method. Comput Phys Commun 181(3):687–702
49. Vial A, Grimault AS, Macías D, Barchiesi D, de la Chapelle ML (2005) Improved analytical fit of gold dispersion: application to the modeling of extinction spectra with a finite-difference time-domain method. Phys Rev B 71:085416
50. Isoyan A, Jiang F, Cheng YC, Cerrina F, Wachulak P, Urbanski L, Rocca J, Menoni C, Marconi M (2009) Talbot lithography: self-imaging of complex structures. J Vac Sci Technol B 27(6):2931–2937
51. Park J, Park JH, Kim E, Ahn CW, Jang HI, Rogers JA, Jeon S (2011) Conformal solid-index phase masks composed of high-aspect-ratio micropillar arrays and their application to 3D nano-patterning. Adv Mater 23:860–864